patterns at 5.23 GHz for the port-1 and port-2 excitations of the antenna with optimal dimensions in this study. Note that the antenna was placed vertically in the anechoic chamber for the measurements, and the receiving antenna is aligned to be parallel to the monopole (1 or 2) under test. That is, the co-polarized component shown in Figure 3 for port-1 excitation is in the direction of $\phi = 135°$; on the other hand, for the port-2 excitation shown in Figure 4, the co-polarized component is in the direction of $\phi = 45°$. From the obtained results, it is seen that the co-polarized radiation for monopole 1 is orthogonal to that for monopole 2, which provides dual-polarized operation for the proposed antenna. The measured radiation patterns in 2.4-GHz band show similar characteristics with those in the 5.2-GHz bands.

4. CONCLUSION

An integrated dual-band diversity antenna has been proposed and studied. The two ports of the antenna show high isolation and have good impedance matching for frequencies across the 2.4-GHz and 5.2-GHz WLAN bands. The antenna can also provide spatial diversity, which capable of combating multipath fading for WLAN operation.

REFERENCES

1. C. Wu, Printed antenna structure for wireless data communications, U.S. Patent no. 6008774, 1999.
2. T.-Y. Wu, S.-T. Fang, and K.-L. Wong, Printed diversity monopole antenna for WLAN operation, Electron Lett 38 (2002), 1625–1626.
3. S.-H. Yeh and K.-L. Wong, Dual-band F-shaped monopole antenna for 2.4 GHz/5.2 GHz WLAN Application, IEEE Antennas Propagat Soc Int Symp, San Antonio, TX, 2002, pp. 72–74.
4. Y.-L. Kuo and K.-L. Wong, Dual-polarized monopole antenna for WLAN application, IEEE Antennas Propagat Soc Int Symp, San Antonio, TX, 2002, pp. 80–82.

ANALYSIS OF MICROSTRIP-TO-CIRCULAR-WAVEGUIDE TRANSITIONS BY A NEW SPATIAL-IMAGES METHOD

F. D. Quesada Pereira, P. Vera Castejón, J. L. Gómez Tornero, D. Cañete Rebenaque, J. Pascual García, and A. Alvarez Melcon
Technical University of Cartagena
Campus Muralla del Mar s/n
30202 Cartagena, Murcia, Spain

ABSTRACT: *In this paper, a new spatial-images procedure has been applied to the analysis of microstrip-to-circular waveguide transitions. The numerical technique is based on the utilization of stratified image rings, from which the weights and orientations of either discrete charges or dipole images are determined. This is accomplished by enforcing the scalar and vector potentials' boundary conditions on the cavity walls. The results obtained with the new Green's functions have been compared to those given by a standard integral-equation method based on the free-space Green's functions, and a finite-element implementation. Good agreement is shown between the different techniques, thus demonstrating the usefulness of the new approach.* © 2005 Wiley Periodicals, Inc. Microwave Opt Technol Lett 45: 563–568, 2005; Published online in Wiley InterScience (www.interscience.wiley.com). DOI 10.1002/mop. 20881

1. INTRODUCTION

Circular waveguides are the base components in many radio-frequency circuits, such as dual-mode filters [1, 2], dielectric resonators filters [3], cavity-backed antennas [4–8], and manifold multiplexers. The use of waveguides is especially important in the high-power stages of transmitters, where very high-power levels are present. When designing components in circular waveguides, a coaxial or microstrip transition is often needed to connect to the rest of the front-end and other processing units of the subsystem [9–11].

In the past, the design of coaxial-to-waveguide transitions were carried out experimentally [12], although the finite-element technique [13], or the finite-difference technique [4] have also been used to study circular-waveguide cavity problems. A more efficient numerical technique is the mode-matching method, which has also been used in the study of irises in circular waveguides [14, 15]. As regards the integral-equation (IE) technique, there are some contributions in which probes or coaxial excitations inside circular waveguides have been numerically studied [16, 11]. Also, the IE technique has been applied to the analysis of circular-cavity-backed antenna problems [7, 8, 10]. In all these contributions, the IE formulates the circular cylindrical Green's functions using its spectral representation in terms of a series of Bessel functions (circular waveguide modes) [17, 18].

Alternatively, one can try to formulate the IE technique using the free-space Green's functions as in [19]. This approach is more involved computationally, since the whole structure, including the cavity walls, needs to be discretized in the numerical model. Consequently, larger systems of equations need to be solved. To overcome the extra computational effort, some authors have developed techniques to render sparse the associated IE matrices [20, 21]. However, these methods are still in a preliminary stage for complex tridimensional problems that involve dielectric and conducting bodies. On the contrary, the spectral-domain Green's function significantly reduces the number of unknowns, which are now limited to the metallic areas of the structure (the Green's functions contain the information of the cavity). This reduction in the number of unknowns, however, is at the expense of a computationally intensive evaluation of higher-order Bessel functions, which might also lead to a lack of precision.

In this contribution, a new numerical procedure, based on the IE method, is used for the analysis of microstrip-to-circular waveguide transitions [22]. The technique makes use, for the first time, of discrete spatial images for the evaluation of the circular-cavity Green's functions. The Green's functions are, therefore, entirely formulated in the space domain. The weights of the images are determined by imposing appropriate boundary conditions to the potentials on the cavity walls. The fulfillment of these boundary conditions along the cavity longitudinal axis is taken into account by considering a discrete number of image stratified rings. One of the advantages of formulating the Green's functions in the space domain, is that the exact same formulation remains valid if one replaces the simple free-space Green's function of a unit dipole image, with another more elaborated spatial domain Green's function. One possibility, for instance, is to use the multilayered media Green's functions formulated as Sommerfeld integrals in the space domain [23]. In this case, it is very simple to automatically take into account the dielectric substrates inside the circular cavity, or even the top and bottom covers of a circular cavity.
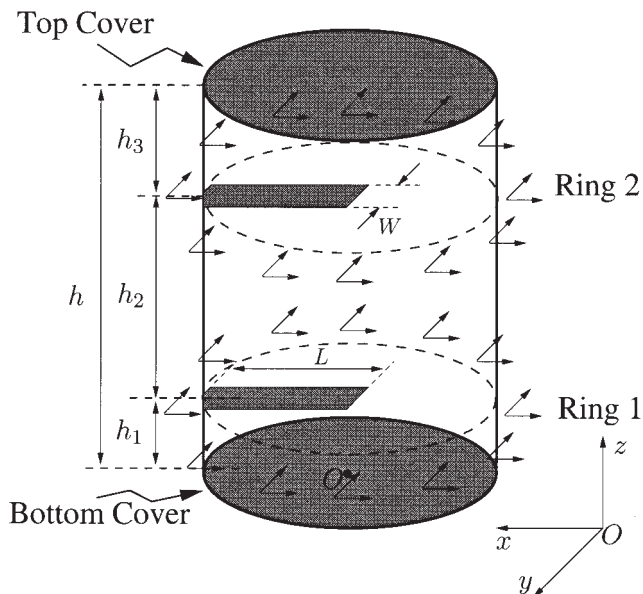
Figure 1 Circular-waveguide-to-microstrip transition with input and output ports ($h_1 = h_2 = h_3 = 5$ mm, $W = 0.5$ mm, $L = 4$ mm, O: origin of coordinates)

The practical use of the technique applied to the analysis of circular-waveguide-to-microstrip transitions is explored in this paper. A novel feature investigated in this paper is the application of the technique when the input and output ports are separated by a large distance. Convergence with the number of image rings are discussed for the first time in this paper. The results obtained using the new technique are validated by comparing them with those obtained using a finite-element technique, and with a standard IE implementation using the free-space Green's function (and consequently discretizing all the cavity walls). Very good agreement is obtained between the three techniques, thus validating this novel approach as a useful numerical technique.
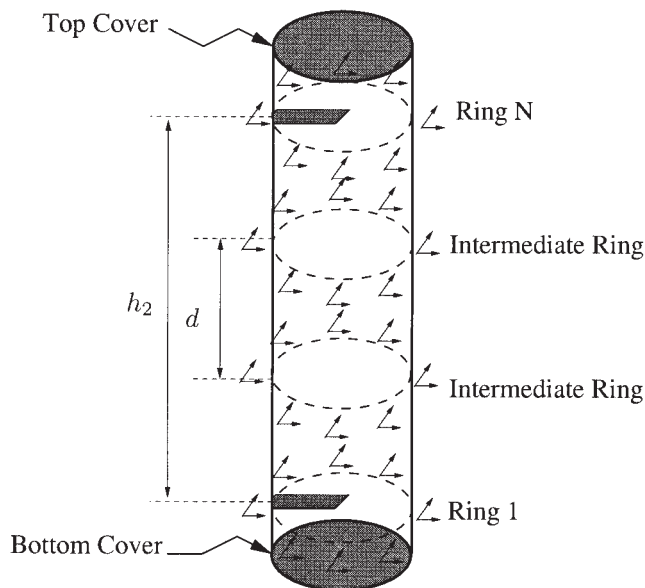
Figure 2 Long circular-waveguide-to-microstrip transition (dimensions are the same as in Fig. 1, but with $h_2 = 20$ mm and distance between image rings: $d = 5.0$ mm
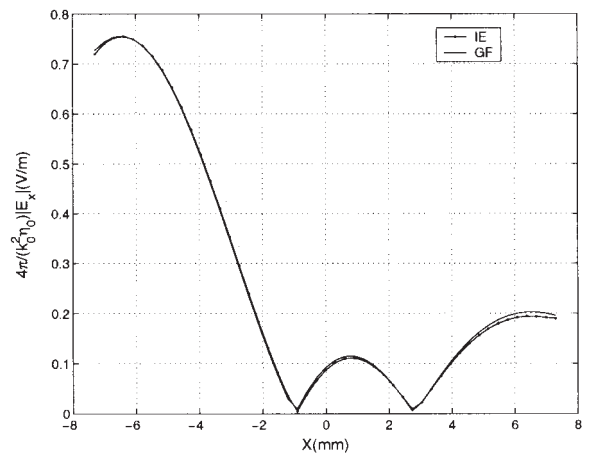

(a)
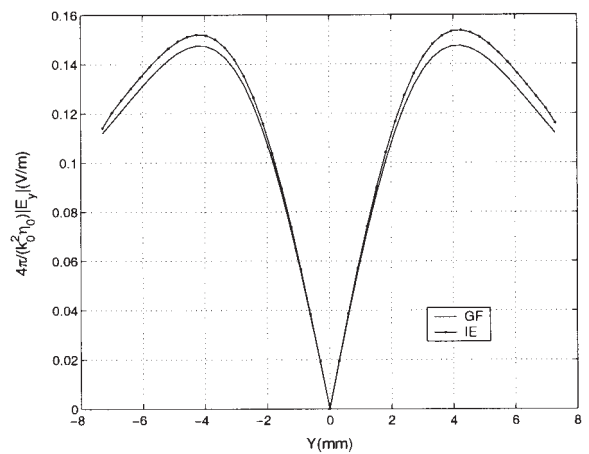
(b)

Figure 3 Electric field produced by an x-directed unit dipole inside the structure of Fig. 1 at frequency $f = 30$ GHz; source is located at ($x'/a = 0.47$, $y'/a = 0$, $z' = h_1$); IE: integral equation with free-space Green's functions; GF: novel cavity Green's functions

2. THEORETICAL OUTLINE

The basic theoretical details of the new spatial-images techniques was presented in [24, 22]. In the first paper [24], a spatial-images procedure to obtain the magnetic vector-potential and the electric scalar-potential Green's functions inside a circular waveguide was presented. In the second paper [22], a similar strategy was used for the evaluation of the electric vector potential and magnetic scalar potential due to magnetic-current sources.

The basic technique uses the free-space Green's function to impose the boundary condition for the potentials at discrete points on the lateral cavity walls. Two system of linear equations are solved to find the weights and orientations of both charges and dipoles images, which are needed to fulfill the required boundary conditions. The same procedure can be used to include layers in the structure, or the top and bottom covers of a circular cavity. This is easily achieved by substituting the free-space Green's functions by the multilayered media Green's functions formulated in the space domain through Sommerfeld integrals [23].
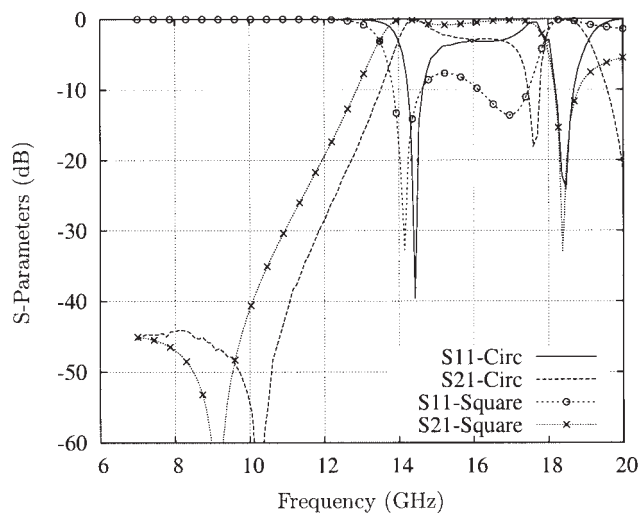
In the original work, the source and observation points used in the calculation of the Green's functions were located at the same cross section. This is because only planar circuits with small cavity
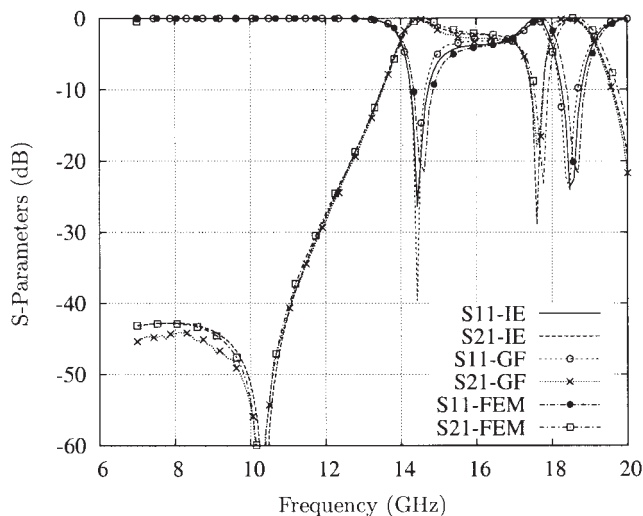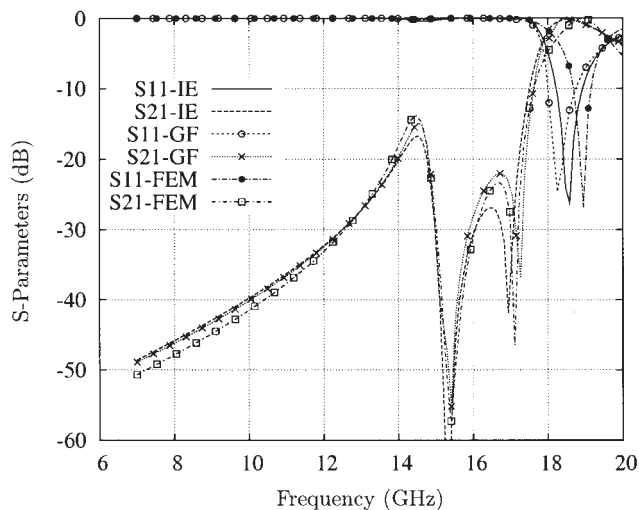
Figure 4 Scattering parameters obtained for the structure shown in Fig. 1 using three different techniques: IE: integral equation with free-space Green's functions; GF: novel cavity Green's functions; FEM: finite-element technique

Figure 6 Scattering parameters obtained for the structure of Fig. 1, but with the output port rotated 90°

heights were used. In this paper, we want to use this technique to investigate circular-waveguide-to-microstrip transitions, containing two ports with a separation of few wavelengths (from λ_0 to $2\lambda_0$). In this case, the coupling between the two ports needs to be computed. Therefore, the Green's functions also need to be evaluated for source and observation points located at different cross-section planes. Also, since the height of the cavity is large, the boundary conditions need to be imposed along the longitudinal axis of the waveguide. This is accomplished by using several rings of images along this axis. This is a new feature of the technique, previously unexplored. The behavior and convergence of the results with respect the number of image rings will be presented, and the achieved accuracy carefully discussed.

In Figure 1, we present a typical situation suitable for the analysis of a structure containing two different metalization levels. A similar situation is used in the analysis of a circular-waveguide-to-microstrip transition, where the input and output ports are placed at two different cross sections. In this case, at least two

rings of images are needed, one at each interface where the ports are located. As shown in Figure 1, the boundary conditions are imposed at discrete points on each one of the two cross sections. Furthermore, if the distance between the two ports is large, the same idea can be generalized, and more intermediate rings of images need to be considered for the sake of accuracy. This idea is illustrated in Figure 2, in the context of the analysis of a circular cylinder of height ($h/\lambda_0 = 2.0$).

3. RESULTS

The technique described in the previous section has been implemented in order to study circular waveguide to microstrip transitions (see Fig. 1). Instead of using the free-space Green's functions, the described procedure has been applied with the space-domain multilayered media Green's functions. In this way, it is simple to take into account for the top and bottom covers of a closed circular cavity. With this technique, then, the computed Green's functions contain all the information relative to the cavity and to the top and bottom covers. Consequently, only the microstrip ports used to couple the energy to the cavity need to be discretized as part of the numerical solution of the IE. Therefore, low numbers of unknowns, leading to very reduced-sized matrices, are obtained, as compared with other techniques such as a finite-element technique or even an IE technique employing the free-space Green's functions.

To demonstrate that the concept of the ring images indeed works, we have computed the electric field produced by a unit dipole inside the circular cavity shown in Figure 1. The source is located at the input port interface, while the electric field is computed along the two main axes at the interface of the output port ($z = h_1 + h_2$). Both source and observation points are, therefore, located at different cross section planes. Two rings of images are used, one at each relevant interface (see Fig. 1). In Figure 3, we compare the electric field obtained with the new Green's functions and with a standard IE technique employing the free-space Green's functions. In this last case the whole cavity wall, including the top and bottom covers, are meshed using triangular cells (4831 basis functions in total). We can observe very good agreement between the two techniques in Figure 3. This demonstrates the validity of the ring-images concept for the effec-

Figure 5 Results obtained for the structure in Fig. 1 inside a circular cavity and inside a square cavity of equal area

TABLE 1   Resonant Frequencies of the Cavity Shown in Fig. 1

Mode Type	Resonant Frequency (GHz)
TM_{010}	15.109
TE_{111}	15.291
TM_{011}	18.118

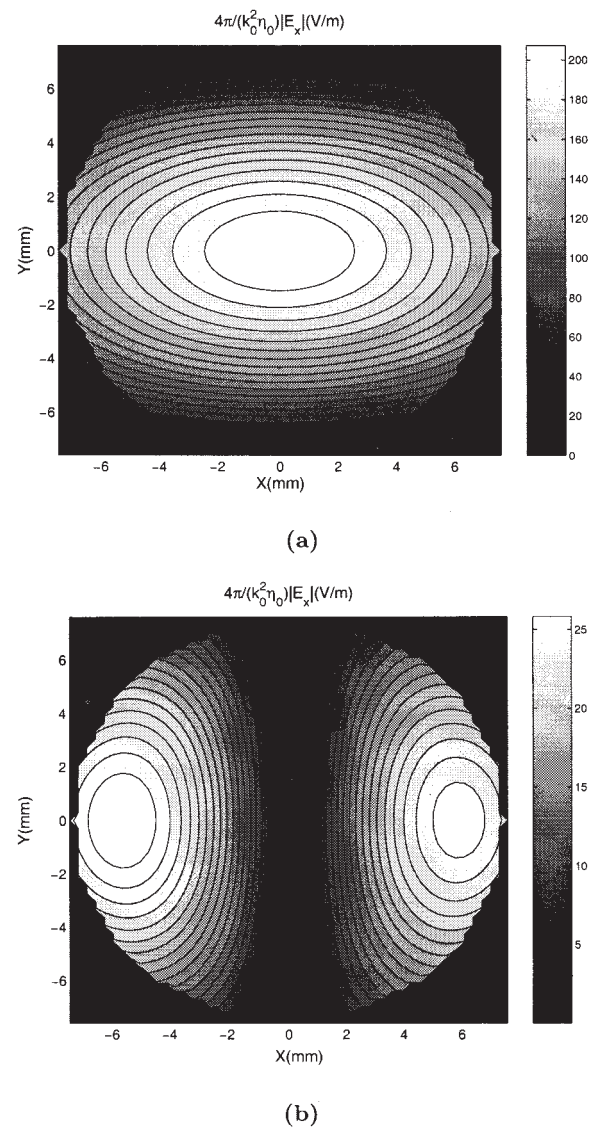tive imposition of the boundary conditions along the height of a thick cavity.

The first real structure investigated in the paper is a circular-waveguide-to-microstrip transition of electrical length equal to one wavelength ($h = \lambda_0$). The details of the geometry are included in Figure 1. The results are obtained using a finite-elements technique, using an IE technique employing the free-space Green's functions, and using an IE technique employing the novel cavity Green's functions. In this last case, only two rings of images are included, with one at each cross section where the probes are placed (Fig. 1). Figure 4 shows (on the same graph) the results obtained using the three approaches. Very good agreement is observed between all results, in spite of using numerical techniques which are intrinsically very different. For this structure, if more rings of images are included in the new Green's functions, essentially the same results are obtained, therefore indicating that convergence has been reached with only two rings.

To show the importance of having an accurate model for a circular waveguide at hand, we include in Figure 5 the results obtained for a square cavity with the same area as that of the circular cavity. The results for the square cavity are obtained using a classical spectral-domain approach [25], while the new Green's functions are used for the circular waveguide. It can be seen that the results are different, but a similar behavior between the square and circular structures is obtained up to 16 GHz. Then the responses of both structures start to be very different. This is due to the excitation and interaction of higher-order modes, which is very different for a circular cavity and for a square cavity. In general, then, the square-cavity model is not suitable to approximate a circular-cavity shape.

To further validate the technique, we have analyzed the rejection for cross polarization of this structure. In this case, the output
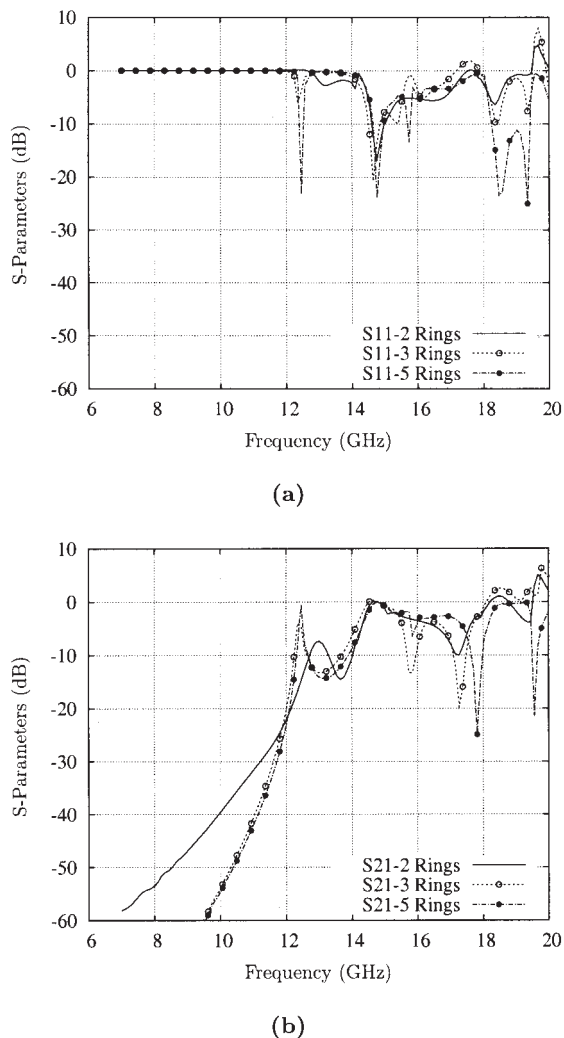

(a)

(b)

Figure 8   Electric-field x-component computed for the structure in Fig. 1 at two resonant frequencies

port is placed at 90° orientation with respect the input port. For the rest, the structure is the same as the one shown in Figure 1. In Figure 6, we present the results obtained using the three techniques previously described. Again, good agreement is observed in this case. In particular, we can also measure a rejection of about −12 dB up to 17 GHz. Then, the rejection is spoilt due to the excitation of higher-order modes, as previously noticed.
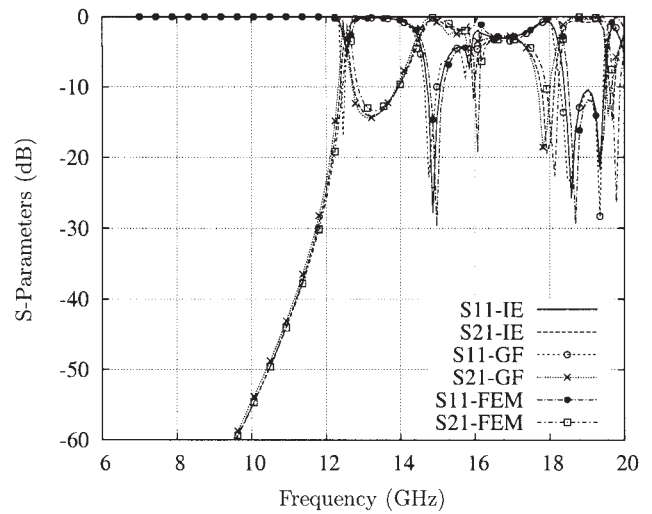
Another interesting phenomenon that has not been reported previously is the presence of some peaks that can be observed at precise frequencies, when the new cavity Green's functions are employed. These peaks in the response are observable in Figures 4, 5, and 6, at frequencies of around 15 GHz and 18 GHz. A straightforward analysis of the empty circular cavity [26] indicates that three resonant frequencies appear at 15.10, 15.29, and 18.11 GHz (Table 1). These correspond exactly to the frequencies where peaks occur in the new cavity Green's functions. To investigate this phenomenon, we have performed a frequency sweep in the potential Green's functions inside the cavity. Figure 7 shows the results obtained for the normalized potential Green's functions, showing peaks at the resonant frequencies of the cavity. Further-

Figure 7   Normalized potential Green's functions in the structure shown in Fig. 1; source position is ($x'/a = 0.47$, $y'/a = 0.47$, $z' = h_1$); observer position ($x/a = -0.47$, $y/a = 0$, $z = h_1 + h_2$)

more, Figure 8 shows the *x*-component of the electric field computed at 15.3 GHz and 18.1 GHz, showing the typical patterns of the circular-waveguide modes. This study indicates that the new Green's functions can detect the natural resonant frequencies of a circular cavity.

The final example investigated is a similar transition as before, but with an electrical height of two wavelengths ($h = 2\lambda_0$). In this case we include, for the first time, a convergence study of the new cavity Green's functions with the number of ring images. This convergence study is shown in Figure 9, where the scattering parameters are presented with two, three, and five rings. We can observe that in this case two rings are not enough to achieve convergence. Also, when three rings are included, the results are only accurate up to a frequency of 15 GHz. On the contrary, with five rings, accurate results are obtained in the whole frequency range up to 20 GHz, as illustrated by the comparison in Figure 10. This last figure presents the results obtained using the three techniques discussed before. The results with the new cavity Green's functions are obtained with five rings of images along the cavity height. Again, good agreement is obtained between the three techniques, thus validating the novel cavity Green's functions. This last result indicates that at least one ring of images is needed

Figure 10 Scattering parameters obtained for the structure shown in Fig. 2 using three different techniques (five image rings are included in the new cavity Green's functions)

per ($\lambda_0/4$) along the height of the cavity in order to achieve good convergence.

4. CONCLUSION

In this paper, we have used a new formulation of the circular-cavity Green's functions for the analysis of circular-waveguide-to-microstrip transitions. The Green's functions are entirely formulated in the space domain, by using a finite series of spatial images. In this way, the computation of Bessel functions of classical spectral-domain formulations are avoided. Novel features of the technique have been presented in this paper, including the imposition of the boundary conditions along the cavity height. This is accomplished by using several rings of images. Convergence of the results with the number of rings along the cavity height has been presented. The results are compared with a finite-element technique and with other IE approaches, showing good agreement. These results validate the novel Green's functions as a useful tool in the analysis and design of devices based on circular cavities or enclosures.

Figure 9 Scattering parameters obtained for the structure in Fig. 2 when different number of image rings are included in the new Green's functions: (a) S_{11} parameter; (b) S_{21} parameter

REFERENCES

1. L. Accatino, G. Bertin, and M. Mongiardo, A four-pole dual mode elliptic filter realized in circular cavity without screws, IEEE Trans Microwave Theory Tech 44 (1996), pp. 2680–2687.
2. P. Guillot, P. Couffignal, H. Baudrand, and B. Theron, Improvement in calculation of some surface integrals: Application to juntion characterization in cavity filter design, IEEE Trans Microwave Theory Tech 41 (1993), 2156–2160.
3. R.R. Mansour, Filter technology for wireless base stations, IEEE Microwave Mag 5 (2004), 68–74.
4. H. Nakano, M. Sugama, and J. Yamauchi, Cavity-backed circular aperture antenna constructed using a triplate transmission line, IEE Proc 146 (1999), 385–390.
5. J. Rubio, M.A. Gonzalez, and J. Zapata, Efficient full-wave analysis of mutual coupling between cavity-backed microstrip patch antennas, IEEE Antennas Wireless Propagat Lett 2 (2003), 155–158.
6. N.C. Karmakar, Investigations into a cavity-backed circular patch antenna, IEEE Trans Antennas Propagat 50 (2002), 1706–1715.
7. F. Zavosh and J.T. Aberle, Single and stacked circular microstrip patch antennas backed by a circular cavity, IEEE Trans Antennas Propagat 43 (1995), 746–750.
8. J.C. Goswami and M. Sachidananda, Cylindrical cavity-backed sus-

pended stripline antenna; theory and experiment, IEEE Trans Antennas Propagat 41 (1993), 1155–1160.

9. G.K.C. Kwan and N.K. Das, Excitation of a parallel-plate dielectric waveguide using a coaxial probe; basic characteristics and experiments, IEEE Trans Microwave Theory Tech 50 (2002), 1609–1620.

10. D.M. Pozar, Analysis and design of cavity coupled microstrip couplers and transitions, IEEE Trans Microwave Theory Tech 51 (2003), 1034–1044.

11. W.W.S. Lee and E.K.N. Yung, The input impedance of a coaxial line fed probe in a cylindrical waveguide, IEEE Trans Microwave Theory Tech 42 (1994), 1468–1473.

12. L. Fan, M.Y. Li, and K. Chang, Circular waveguide to microstrip transitions, Electron Lett 31 (1995), 294–295.

13. R.-B. Wu, A wideband waveguide transition design with modified dielectric transformer using edge-based tetrahedral finite-element analysis, IEEE Trans Microwave Theory Tech 44 (1996), 1024–1031.

14. L. Accatino and G. Bertin, Design of coupling irises between circular cavities by modal analysis, IEEE Trans Microwave Theory Tech 42 (1994), 1307–1313.

15. R. Keller and F. Arndt, Rigorous modal analysis of the asymmetric rectangular iris in circular waveguides, IEEE Microwave Guided Wave Lett 3 (1993), 185–187.

16. B.-S. Wang, Mutual impedance between probes in a circular waveguide, IEEE Trans Microwave Theory Tech 37 (1989), 1006–1011.

17. A.H. Mohammadian, Time-dependent dyadic Green's functions for rectangular and circular waveguide, IEEE Trans Antennas Propagat 36 (1988), 369–375.

18. E.L.T. annd S.Y. Tan, Dyadic Green's functions for circular waveguides filled with biisotropic media, MTT 47 (1999), 1134–1137.

19. F.Q. Pereira and A.A. Melcon, Analysis of finite microstrip structures using an efficient implementation of the integral equation technique, IEEE Int Microwave Symp, Philadelphia, PA, 2003, pp. 1983–1986.

20. A. Vidal, A. Belenguer, H. Esteban, V.E. Boria, C. Bachiller, and M. Taroncher, Efficient and accurate spectral analysis of large scattering problems using wavelet and wavelet-like bases, Radio Sci 39 (2004), 5.1–5.17.

21. W.C. Chew, J.M. Song, and E. Michielssen, A succint way to diagonalize the translation matrix in three dimensions, Microwave Opt Technol Lett 15 (1997), 144–147.

22. F.Q. Pereira, P.V. Castejon, D.C. Rebenaque, J.P. Garcia, and A.A. Melcon, Numerical evaluation of the Green's functions for cylindrical enclosures, IEEE Trans Microwave Theory Tech 53 (2005).

23. J.R. Mosig and A.A. Melcon, Green's functions in lossy layered media: Integration along the imaginary axis and asymptotic behavior, IEEE Trans Antennas Propagat 51 (2003), 3200–3208.

24. P.V. Castejon, F.Q. Pereira, D.C. Rebenaque, J.P. Garcia, and A.A. Melcon, Numerical evaluation of the Green's functions for cylindrical enclosures by a new spatial images method, IEEE Int Microwave Symp, Fort Worth, TX, 2004.

25. A.A. Melcon, J.R. Mosig, and M. Guglielmi, Efficient CAD of boxed microwave circuits based on arbitrary rectangular elements, IEEE Trans Microwave Theory Tech 47 (1999), 1045–1058.

26. C.A. Balanis, Advanced engineering electromagnetics, Wiley, New York, 1989.

USE OF A NOVEL WIDE-ANGLE FD-BPM FOR LOSS PERFORMANCE ASSESSMENT IN RANDOMLY PERTURBED PHOTONIC CRYSTAL FIBERS

V. E. Nascimento, C. A. De Francisco, D. H. Spadoti, M. A. Romero, and B. V. Borges
Electrical Engineering Department
University of São Paulo
Av. Dr. Carlos Botelho
1465, 13560-250 São Carlos-SP, Brazil

ABSTRACT: *A novel wide-angle finite-difference beam-propagation method is applied to the analysis of confinement losses in photonic crystal fibers (PCFs). The method is formulated in terms of the locally one-dimensional (LOD) technique and Padé polynomials. It was found that the wide-angle approach allows an acceleration of the convergence rate of up to 50% for the effective-index imaginary part when compared to paraxial formalism. In this framework, an important aspect of PCF structures, namely, the random structural variation of the hole radius and pitch, which occurs during the fabrication process of these devices, is investigated in this paper.* © 2005 Wiley Periodicals, Inc. Microwave Opt Technol Lett 45: 568–573, 2005; Published online in Wiley InterScience (www.interscience.wiley.com). DOI 10.1002/mop.20882

1. INTRODUCTION

Photonic crystal fibers (PCFs) are indeed one of the most extraordinary structures recently developed for lightwave propagation. These fibers possess quite interesting adjustable properties such as dispersion, mode size, anomalous group dispersion, and so on [1–3]. In the past few years, a great deal of attention has been dedicated to confinement-loss calculation for these structures, aiming at commercial applications [4–8]. PCFs are usually single-material fibers, with the outermost region (the region surrounding the rings of holes) presenting the same refractive index as the solid-core region. Consequently, all propagating modes are considered leaky modes with complex propagation constants. The imaginary part of the propagation constant gives the magnitude of the confinement losses.

It has been shown that the confinement loss has a direct dependence upon the number of holey rings surrounding the PCF core. An in-depth investigation of this dependence was carried out with the full vectorial multipole (FVM) approach for different numbers of hole ring and several hole diameters [4]. This dependence was also investigated with the same approach by Finazzi et al. [8] for PCF structures consisting of two and three rings. A scalar wave approach has also been utilized to calculate confinement loss based on the Fourier decomposition method (FDM) [5]. As opposed to the FVM approach, this method is not limited to circular holes; however, both FVM and FDM are not beam-propagation methods. Another method that has also been successfully applied to the confinement-loss calculation is the full-vectorial imaginary-distance finite-element BPM based on curvilinear edge/nodal hybrid elements [6].

Three-dimensional beam propagation methods (3D-BPM) can in fact be utilized for confinement loss calculation but, as pointed out in [4], they require considerably large propagation distances. This difficulty, as will be discussed subsequently, can be alleviated through the utilization of wide-angle techniques. The ability to